Solar Energy 302 (2025) 113991

Contents lists available at ScienceDirect

Solar Energy

journal homepage: www.elsevier.com/locate/solener

# Improved satellite-based estimation of direct normal solar irradiance using clearness index with deep learning methods

Shanlin Chen [a], Tao Jing [b], Mengying Li [b], Hiu Hung Lee [a], Siqi Bu [a,c,*]

[a] Centre for Advances in Reliability and Safety, Hong Kong Special Administrative Region
[b] Department of Mechanical Engineering, The Hong Kong Polytechnic University, Hong Kong Special Administrative Region
[c] Department of Electrical and Electronic Engineering, The Hong Kong Polytechnic University, Hong Kong Special Administrative Region

ARTICLE INFO

Dataset link: https://gml.noaa.gov/aftp/data/radiation/surfrad/, https://noaa-goes16.s3.amazonaws.com/index.html, https://nsrdb.nrel.gov/data-viewer

*Keywords:*
Satellite-to-irradiance
Direct normal irradiance
Clearness index
Deep learning

ABSTRACT

As the capacity addition of solar energy systems continues to increase, solar resource assessment is necessary in supporting the feasibility study. This can reduce associated risks of solar energy projects and improve their reliability. Considering the scarcity of on-site measurements, satellite-based irradiance retrievals with high temporal resolutions (i.e., 5-min) have been extensively used as an alternative in solar resource assessment. However, satellite-to-irradiance algorithms, either physical or statistical, focus more on the global horizontal irradiance. The direct normal irradiance (DNI) in most satellite-derived irradiance products is associated with more uncertainties because of its high sensitivity to the atmosphere. To further improve the accuracy in end-to-end satellite-based 5-min DNI estimations, the clearness index based on extraterrestrial solar irradiance is proposed as the target in deep learning satellite-to-DNI models with images of eight selected spectral bands. The results show that clearness index can better account for attenuation effects of the atmosphere, and thus the DNI estimations are associated with lower uncertainties. The use of clearness index offers additional advantages on computing extraterrestrial solar irradiance and pre-processing 5-min spectral satellite data, which is beneficial for large-scale applications. Although the satellite-to-DNI estimation shows high errors under clear-sky condition at some stations, and more efforts are still required in better extracting the atmospheric information (e.g., clouds and aerosols) from satellite images, especially at low solar elevations, the clearness index provides a new perspective in 5-min satellite-to-DNI retrievals with reduced uncertainties. This is beneficial to the reliability in designing solar energy projects.

## 1. Introduction

With the growing need of clean energy, it is expected that the capacity of renewables will keep increasing as driven by the reduced costs, supportive policies, and global climate goals [1,2]. It is reported that the new capacity addition of solar power by 2030 will account for 80% of the global growth of renewable energy [3]. However, the power output and reliability of solar photovoltaic (PV) and concentrated solar power (CSP) are heavily relied on the available solar irradiance, namely, global horizontal irradiance (GHI), direct normal irradiance (DNI), and diffuse horizontal irradiance (DHI). The uncertainty and intermittency of local solar irradiance, as one of the major challenges in the application of solar energy systems, greatly hinders their operation and integration to the power grid [4]. Therefore, it is necessary to have adequate on-site information (e.g., solar irradiance) for solar resource assessment to support the feasibility study of solar energy projects, which is to reduce the long-term risk and ensure the reliability [5]. Calibrated ground measurements are usually the most reliable data source, while complete and long-term in-situ measurements are scarce at most locations because of the financial and technical constraints [4]. Under such circumstances, irradiance retrievals from satellite measurements have been widely used as an alternative in supporting the design of solar energy projects [6,7].

Algorithms for satellite-based irradiance estimation can be broadly classified as statistical and physical methods [5,7]. Physical methods employ radiative transfer models (RTMs) to simulate the interaction between solar radiation and atmospheric compositions. Compared with physical methods, pure empirical and semi-empirical statistic methods are generally easier to implement. Physical and semi-empirical models can be accurate as long as there are high-quality atmospheric inputs

* Corresponding author at: Department of Electrical and Electronic Engineering, The Hong Kong Polytechnic University, Hong Kong Special Administrative Region.
*E-mail address:* siqi.bu@polyu.edu.hk (S. Bu).

https://doi.org/10.1016/j.solener.2025.113991
Received 10 June 2025; Received in revised form 23 August 2025; Accepted 10 September 2025
Available online 22 September 2025

## Nomenclature

### Abbreviations

| | |
|---|---|
| ABI | Advanced Baseline Imager |
| BON | Bondville |
| CNN | Convolutional neural network |
| CSP | Concentrated solar power |
| DHI | Diffuse horizontal irradiance |
| DNI | Direct normal irradiance |
| $DNI_{cs}$ | Clear-sky DNI |
| DRA | Desert Rock |
| FPK | Fort Peck |
| GHI | Global horizontal irradiance |
| $GHI_{cs}$ | Clear-sky GHI |
| GOES | Geostationary Operational Environmental Satellite |
| GWN | Goodwin Creek |
| $Irradiance_{cs}$ | Clear-sky solar irradiance |
| MBE | Mean bias error |
| MERRA-2 | Modern-Era Retrospective analysis for Research and Applications, Version 2 |
| NIR | Near-infrared |
| nMBE | Normalized mean bias error |
| nRMSE | Normalized root mean squared error |
| NSRDB | National solar radiation database |
| POA | Plane of array |
| PSM | Physical solar model |
| PSU | Pennsylvania State University |
| PV | Photovoltaic |
| QC | Quality control |
| ReLU | Rectified Linear Unit |
| RMSE | Root mean squared error |
| RTM | Radiative transfer model |
| SURFRAD | Surface Radiation Budget Network |
| SXF | Sioux Falls |
| SZA | Solar zenith angle |
| TBL | Table Mountain |
| UTC | Coordinated Universal Time |

### Notations

| | |
|---|---|
| $*$ | Convolution operator |
| $\bar{o}$ | Mean of the observation |
| $\lambda$ | Wavelength |
| $\mu$ | Mean |
| $\sigma$ | Standard deviation |
| $\theta$ | Solar zenith angle |
| $\tilde{L}$ | Normalized pixel value |
| $^\circ$ | Degree |
| $d$ | Dimension |
| $e$ | Estimation |
| $E_0$ | Extraterrestrial solar irradiance |
| $E_{sc}$ | Solar constant |
| $f$ | Function |
| $K$ | Key |
| $kc$ | Clear-sky index of GHI |
| $kcb$ | Clear-sky index of DNI |
| $ktb$ | Clearness index of DNI |
| $ktb$_T | Transferred model based on $ktb$ |
| $ktb$_UNS | Clearness index with unnormalized satellite data |
| $ktb$_UNST | Transferred model based on $ktb$_UNS |
| $L$ | Raw pixel value |
| $N$ | Number of data points |
| $o$ | Observation |
| $Q$ | Query |
| $R^2$ | Coefficient of determination |
| $raw$ | Pack-scaled value |
| $scale$ | Scale factor |
| $t$ | Time |
| $V$ | Value |
| $W_i$ | Weights |
| $offset$ | Add offset |
| $radiance$ | Radiance received by satellite sensor |

### Subscripts

| | |
|---|---|
| $i$ | The $i$th row |
| $j$ | The $j$th column |
| $k$ | The $k$th value |
| $t$ | Time |

### Superscripts

| | |
|---|---|
| $b$ | Spectral channel |

available, though such inputs are difficult to obtain. Given advancements of machine and deep learning algorithms and the improved resolution of spatio-temporal data from modern geostationary satellites, the combination of deep learning and remote sensing has been applied as an optimized statistical method for satellite-to-irradiance applications [8]. Even the national solar radiation database (NSRDB) has applied machine learning with physical guidance to improve the quality and accuracy of the irradiance retrieval data [9,10]. The combination of remote sensing and deep learning can better extract the cloud information from satellite images and thus the uncertainty in solar irradiance estimation can be reduced [8]. Although end-to-end deep learning satellite-to-irradiance methods are more effective in implementation, they often face extrapolation issues, where physics-informed machine learning could be a solution.

Both GHI and DNI are important components for quantifying the available surface solar irradiance for energy applications [4]. Compared with GHI, DNI is more related to CSP or PV with a tracking system [11]. In fact, DNI is also an important component in the calculation of the plane of array (POA) irradiance for inclined PV panels at a fixed angle [12]. There are many methods proposed for solar irradiance retrieval from different satellites apart from the NSRDB, for instance, the physics-based and empirically adjusted algorithm based on the SEVIRI satellite [13], the physical Heliosat−4 method [14] based on Meteosat Second Generation satellites, and machine learning methods with satellite data from Himawari-8 [15] and Fengyun-4 [16]. It has been repeatedly observed that satellite-based DNI estimations, derived with either physical or data-driven models, are associated with higher uncertainties than satellite-to-GHI retrievals [8,17]. The possible reason could be that DNI is more sensitive to the atmosphere than GHI, as the attenuation of sunlight in the incoming direction is more influenced by clouds (via blocking) [11], while GHI is partially compensated by the increased DHI because of scattering through the closure relationship. As the most frequently used irradiance component, GHI is usually the target of interest in satellite-based estimation of solar irradiance [5]. In practical applications, GHI can be separated to DNI and DHI with a separation model [18], or transposed to POA irradiance using a

transposition model [19]. However, there might be some accumulated error in irradiance separation and transposition using satellite-derived GHI [20]. To better support satellite-based solar resource assessment for both PV and CSP projects, it is necessary to obtain satellite-derived DNI with reduced uncertainties [11].

Since the inputs of cloud properties (as the most influential factor) for RTM-based DNI calculation are usually derived from satellite measurements [9], there has been a dearth of studies to reduce error accumulations in RTM-based satellite-to-DNI and to improve the modeling efficiency. In physical satellite-to-DNI models, the key is to improve the representation of DNI from satellite measurements [20,21]. For clear sky conditions, DNI is usually computed using with clear-sky models (e.g., the REST2 [22] and McClear [23]) with atmospheric inputs, such as Moderate Resolution Imaging Spectroradiometer [9] and Modern-Era Retrospective analysis for Research and Applications, Version 2 (MERRA-2) [11,20]; while in cloudy skies, clouds attenuation on DNI is usually determined using satellite data. For instance, the cloud cover [21] or cloudiness index (representing the cloud effect on DNI) [20] can be derived from visible imagery of geostationary satellite, such as the Geostationary Operational Environmental Satellite (GOES), which is then coupled with clear-sky models (e.g., REST2) and atmospheric inputs (e.g., MERRA-2) to calculate DNI estimates under all-sky conditions [20,21].

Although physical methods are universal and could have very high accuracies with detailed atmospheric concentration profiles, while such information are usually difficult to obtain. On the other hand, deep learning models can be used as an alternative to replace physical methods for satellite-to-irradiance conversion with appropriate hyperparameters, adequate observations, and effective training [24,25]. In satellite-based solar irradiance estimation with machine learning, satellite data should be pre-processed or normalized [1]. This is applicable to both solar resource assessment [8] and forecasting that directly using satellite data [26], and those indirect solar radiation modeling involved with cloud detection [27] and cloud motion forecast [28]. Similarly, the target in data-driven satellite-based solar resource assessment should also be normalized. The output is usually the clear-sky index (Irradiance/Irradiance$_{cs}$) [8,29], which is the ratio between irradiance measurements and their clear-sky expectations (Irradiance$_{cs}$). However, clear-sky models generally show higher uncertainties in clear-sky DNI computations because of the uncertainties in atmospheric inputs [30], which means clear-sky index of DNI based on inaccurate clear-sky DNI expectation might not account for the true cloud attenuation effect. It is on this account that this study proposes to use clearness index in satellite-to-DNI with deep learning to reduce the uncertainty in DNI estimations. The major contributions of this work are summarized as follows:

- Clearness index of DNI based on extraterrestrial solar irradiance is proposed in satellite-based DNI estimations with deep learning. This provides a more efficient method for normalizing DNI time series than clear-sky DNI normalization, since the extraterrestrial solar irradiance is more convenient to compute, which also avoids the uncertainties in clear-sky DNI models.
- Clearness index also has the advantage over clear-sky index in accuracy, as extraterrestrial solar irradiance can be calculated with a high accuracy, whereas clear-sky DNI estimations are often associated with large modeling uncertainties. Additionally, clearness index inherently accounts for attenuation effects on DNI of all atmospheric compositions along the direct optical path, which provides a more comprehensive representation of the atmospheric influence on DNI than the clear-sky index.
- The impact of satellite data normalization is investigated in deep learning based satellite-to-DNI modeling, which demonstrates that clearness index better reflects the atmospheric attenuation effect and is more compatible with raw satellite inputs. The saved efforts in extensive satellite data pre-processing can further improve the modeling efficiency, particularly beneficial for large-scale regional applications.

The rest of this work is structured as follows: Section 2 describes the used data of ground-level measurements, satellite images, and satellite-derived irradiance with physical methods. Data pre-processing and deep learning satellite-to-DNI method are detailed in Section 3. The results of satellite-based DNI estimations are evaluated and compared in Section 4. Finally, the key findings of this study are summarized in Section 5.

## 2. Data

### 2.1. Ground-level measurements

Ground-level measurements used in this work are from the Surface Radiation Budget Network (SURFRAD) [31], which consists of seven stations, namely, Bondville (BON), Desert Rock (DRA), Fort Peck (FPK), Goodwin Creek (GWN), Penn. State University (PSU), Sioux Falls (SXF), and Table Mountain (TBL), in several climate zones across the United States. A detailed illustration of the seven SURFRAD stations is presented in Fig. 1 and Table 1. SURFRAD provides high-quality 1-min data for a variety of meteorological measurements indexed with Coordinated Universal Time (UTC). Although the major variable of interest is DNI for model development and performance evaluation, other types of data, including GHI, DHI, solar zenith angle (SZA), are required for quality control (QC). All the mentioned 1-min data from years 2019 and 2020 are downloaded and filtered using a couple of QC steps, namely, extremely rare limit test and three-component closure test [32]. There are three parts in the extremely rare limit test:

$$-2 \le \mathrm{GHI} \le 1.2E_0\cos^{1.2}(\theta) + 50, \tag{1}$$

$$-2 \le \mathrm{DHI} \le 0.75E_0\cos^{1.2}(\theta) + 30, \tag{2}$$

$$-2 \le \mathrm{DNI} \le 0.95E_0\cos^{0.2}(\theta) + 10, \tag{3}$$

where $E_0$ [W/m$^2$] is the extraterrestrial solar irradiance, $\theta$ [°] is the SZA. The three-component closure test has two steps:

$$|\ \mathrm{closure}\ | \le 8\% \text{ for } \theta \le 75^\circ \text{ and } \mathrm{GHI} > 50, \tag{4}$$

$$|\ \mathrm{closure}\ | \le 15\% \text{ for } 75^\circ < \theta < 93^\circ \text{ and } \mathrm{GHI} > 50, \tag{5}$$

where $\mathrm{closure} = \mathrm{GHI}/(\mathrm{DNI}\cdot\cos(\theta) + \mathrm{DHI}) - 1$, which describes the closure relationship of the three solar irradiance components. Any data points that cannot pass the QC steps are removed. For more details and theoretical aspects on the QC steps in pre-processing raw solar irradiance measurements, the reader is referred to [32,33]. Since solar irradiance is not available during nighttime and there is a high air mass effect at solar mornings and evenings [34], irradiance measurements at a SZA of 85° or greater are discarded. After QC, the 1-min data are resampled to 5-min intervals using the 'center' scheme, as suggested by [17,35,36]. For example, the 5-min DNI at $t$ = 14:00 is the mean over times of 13:58, 13:59, 14:00, 14:01, and 14:02.

### 2.2. Satellite data

Geostationary satellites collectively cover all areas within latitudes of ±60°, providing continuous observations of atmospheric conditions for the Earth [2]. There are a variety of data and data products from measurements of the geostationary satellite. For instance, GOES-R series provide numerous Level 1b and Level 2 products for different applications. The satellite data used in this work are spectral imagery of GOES-16 located at the operational longitude of 75.2°W during the investigated period of this study. These spectral images are based on the measured radiance (Level 1b data) that have been calibrated and georeferenced. There are 16 spectral bands in the Advanced Baseline Imager (ABI) of GOES-16, which can provide measurements in the temporal resolution of 5-min and in the spatial resolution of 0.5–2 km

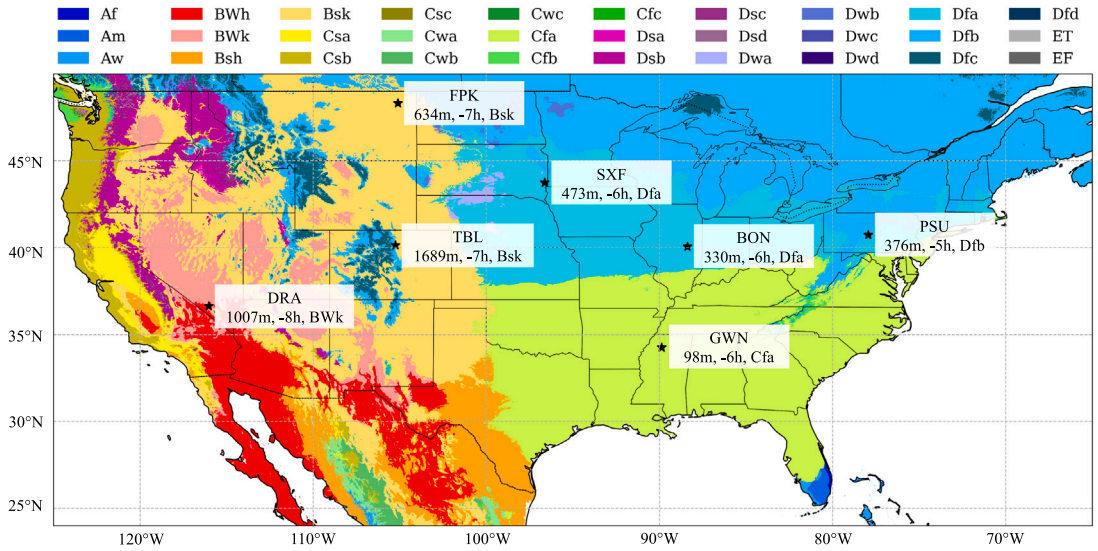


**Fig. 1.** Spatial distribution of the seven SURFRAD stations. The information in brackets is (altitude [m], time difference from UTC [hours], climate zones), where the climate zone in different color is based on Köppen-Geiger climate classifications [37]. (For interpretation of the references to color in this figure legend, the reader is referred to the web version of this article.)

**Table 1**
A summary of the seven SURFRAD stations. The climate is based on Köppen classifications: Bsk (arid, steppe, cold), Bwk (arid, desert, cold), Cfa (temperate, without dry season, hot summer), Dfa (continental, without dry season, hot summer), Dfb (continental, without dry season, warm summer).

| Abbr. | Station | Latitude | Longitude | Altitude | Climate | Time zone | Data available[a] |
|---|---|---|---|---|---|---|---|
| BON | Bondville | 40.05° | −88.37° | 230 m | Dfa | UTC-6 | 36.65% |
| DRA | Desert Rock | 36.62° | −116.02° | 1007 m | Bwk | UTC-8 | 38.25% |
| FPK | Fort Peck | 48.31° | −105.10° | 634 m | Bsk | UTC-7 | 34.58% |
| GWN | Goodwin Creek | 34.25° | −89.87° | 98 m | Cfa | UTC-6 | 35.01% |
| PSU | Penn. State Uni. | 40.72° | −77.93° | 376 m | Dfb | UTC-5 | 34.68% |
| SXF | Sioux Falls | 43.73° | −96.62° | 473 m | Dfa | UTC-6 | 32.80% |
| TBL | Table Mountain | 40.12° | −105.24° | 1689 m | Bsk | UTC-7 | 36.41% |

[a] All nighttime data and points that do not pass the quality control are discarded.

at the sub-satellite point for the continental United States. The radiance products of all 16 channels can be used individually or together for applications on analyzing the Earth and atmosphere [38]. For instance, reflective bands (1–6) are for the characterization of clouds, vegetation, snow/ice, and aerosols, while emissive bands (7–16) can support characterizing the surface, clouds, water vapor, and particles that based on emissive properties [39]. In principle, all 16 satellite spectral bands should be used in deep learning based satellite-to-DNI models since they characterize different atmospheric constituents. However, it is also essential to remove redundant features in machine/deep learning applications. Therefore, only a subset of eight representative channels (see Table 2) are used due to the high correlations of some bands [8]. This is to reduce efforts in pre-processing satellite data and to improve the learning efficiency. In a more general case, one could further reduce the number of used spectral channels to investigate the effects on DNI estimations, but this is not within the scope of this work.

Spectral GOES-16 images of the eight bands with the time resolution of 5-min in years of 2019 and 2020 are extracted for the seven target SURFRAD stations. These images are sized at 11 × 11 pixels with the target station in the center, following the steps detailed in [8,29]. Note that there is a tradeoff between the spatial scale and computing efficiency, and the improvement of modeling accuracy becomes marginal with large spatial size of satellite images [40]. Therefore, the use of 11 × 11 pixels is adopted following several studies on satellite-based solar irradiance modeling [8,41] and cloud detection [27]. The packed-scaled satellite measurements of each spectral band are converted to radiance using 'scale factor' and 'add offset' shown in Table 2 ($radiance = raw \times scale + offset$, where $raw$ is the packed-scaled value). Note that the ABI is a multi-channel passive imaging radiometer, so the radiance received should not be less than zero. Therefore, spectral images with any negative radiance values are discarded. Since there are different spatial resolutions for the spectral bands (1–2 km as shown in Table 2), measurements of spectral channels with finer resolutions are re-scaled to 2-km. To be compatible with ground-level irradiance measurements, the end-of-scan timestamps in UTC, rounded to the next nearest 5-min interval (although with some inaccuracies), are used to index the spectral satellite images [8,29]. Some sample spectral images of the eight selected bands are presented in Fig. 2, for one of the target SURFRAD stations.

### 2.3. NSRDB data

As the state-of-the-art in satellite-based estimation of ground-level solar irradiance, NSRDB provides publicly available satellite-derived solar irradiance that can be applied in situations where the on-site measurements are not available [9]. NSRDB also provides many auxiliary variables (e.g., SZA, cloud type, and meteorological data), which can be accessed via https://nsrdb.nrel.gov/. The geographical coverage of NSRDB includes the United States and the number of other international locations is still growing [9,10]. NSRDB employs a physical solar model (PSM) to calculate solar radiation from satellite-derived cloud properties and data products (e.g., aerosol and water vapor) from a number of other associations [9]. As a serially complete database, NSRDB provides data with a coverage of more than 20 years. Using the high-resolution data from GOES-16 and -17, the spatio-temporal resolution of NSRDB has been improved to 5-minute–2-km since 2018, which

**Table 2**
Detailed description of the eight selected ABI spectral bands of GOES-16. The resolution is defined at the sub-satellite point. Channel types include visible, near-infrared (NIR), and infrared. Valid range is the range of packed-scaled value of satellite measurement, which can be converted to radiance using the scale factor and add offset. The nickname refers its characteristics for different applications.

| Channel | $\lambda$ (center $\lambda$) [μm] | Resolution [km] | Type | Valid range | Scale factor (Add offset) | Nickname |
|---|---|---|---|---|---|---|
| 1 | 0.45–0.49 (0.47) | 1 | Visible | 0–1022 | 0.8121 (−25.9366) | Blue |
| 3 | 0.846–0.885 (0.865) | 1 | NIR | 0–1022 | 0.3769 (−20.2899) | Veggie |
| 4 | 1.371–1.386 (1.378) | 2 | NIR | 0–2046 | 0.0707 (−4.5224) | Cirrus |
| 5 | 1.58–1.64 (1.61) | 1 | NIR | 0–1022 | 0.0958 (−3.0596) | Snow/Ice |
| 6 | 2.225–2.275 (2.25) | 2 | NIR | 0–1022 | 0.0301 (−0.9610) | Cloud particle size |
| 7 | 3.80–4.00 (3.90) | 2 | Infrared | 0–16 382 | 0.0016 (−0.0376) | Shortwave window |
| 9 | 6.75–7.15 (6.95) | 2 | Infrared | 0–2046 | 0.0225 (−0.8236) | Mid-level water vapor |
| 11 | 8.30–8.70 (8.50) | 2 | Infrared | 0–4094 | 0.0334 (−1.3022) | Cloud-top phase |

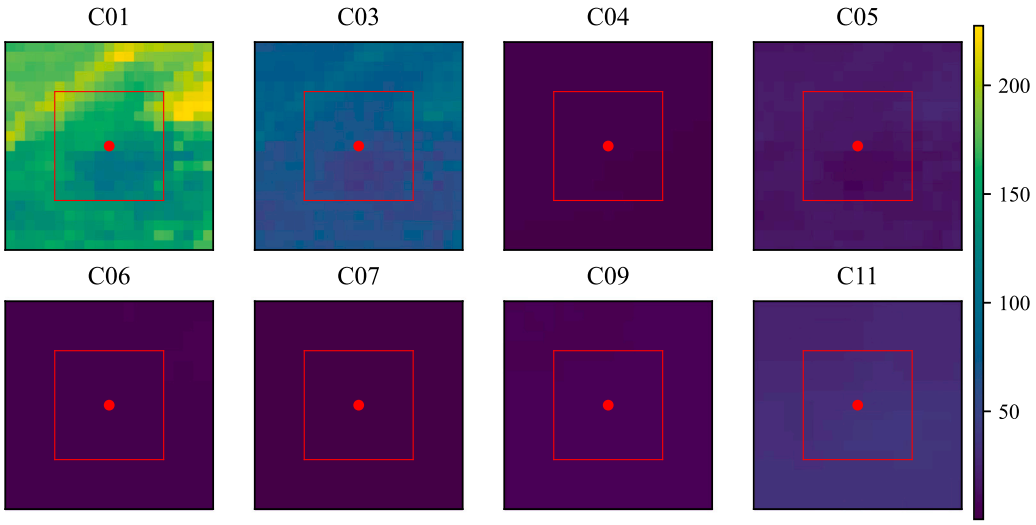


**Fig. 2.** Sample raw GOES-16 images of the eight selected spectral for the Bondville (BON) station (40.05°, −88.37°) at 2020-01-13 18:30:00 (UTC). The whole images are sized of 21 × 21 pixels, where interested region is in the square of 11 × 11 pixels with BON (red point) located at the center. (For interpretation of the references to color in this figure legend, the reader is referred to the web version of this article.)

was 30-minute–4-km before. The validation of 5-min irradiance data from NSRDB shows higher discrepancies due to the improved temporal resolution, for instance, Yang [17] reported that 5-min NSRDB GHI and DNI at SURFRAD stations have the normalized root mean squared error (nRMSE) in the range of 14.87%–38.33% and 21.11%–48.78%, respectively, in years of 2018 and 2019. However, the accuracy of DNI estimates in NSRDB has been enhanced with better cloud parameterizations based on satellite data [11] and an improved DNI model under cloudy conditions [42,43]. This makes the 5-min NSRDB an important part in modern solar irradiance modeling and resource assessment.

Since NSRDB is based on the PSM with improved accuracy and availability, it has been extensively used in solar energy applications [9] and as benchmarks [8,29]. The 5-min DNI values and clear-sky DNI expectations from the most recent version of NSRDB [11] in years 2019 and 2020 are downloaded for all SURFRAD stations. The clear-sky DNI in NSRDB is obtained using the REST2 model [9,22], which is identified as one of the high-performance clear-sky models [44]. The 5-min NSRDB DNI is used to benchmark the proposed satellite-to-DNI method due to its recent enhancements [11], and the clear-sky DNI estimation is applied to normalize the DNI measurements, which is detailed in Section 3.1. Note that NSRDB and satellite-to-DNI estimation using deep learning are both satellite-derived irradiance products, although site-adaptation can improve the accuracy, this is not considered in this study.

## 3. Satellite-to-DNI with deep learning

Owing to the improvement of both computational ability and learning algorithms, deep learning has been extensively used in solar irradiance estimation from satellite measurements [8,45]. Compared with physical satellite-to-irradiance methods, for example, the PSM in NSRDB, deep learning offers simpler but more efficient representations in modeling the interaction between solar radiation and the atmosphere, especially when using spectral satellite images [8]. In the deep learning model for solar irradiance estimation using satellite data, the typical inputs are multi-spectral satellite images that can provide information for various atmospheric compositions (e.g., cloud, aerosol, and water vapor), and the output is usually the clear-sky index [1,8]. The clear-sky index, as the ratio of irradiance measurement and its clear-sky expectation, is to remove the double-pattern seasonality of irradiance [8,46]. The clear-sky index is mainly applied to GHI normalization, as defined by:

$$kc = \mathrm{GHI}/\mathrm{GHI}_{\mathrm{cs}}, \tag{6}$$

where kc is the clear-sky index, $\mathrm{GHI}_{\mathrm{cs}}$ [W/m$^2$] is the clear-sky GHI estimation.

### 3.1. Clear-sky index and clearness index for DNI

Similar to clear-sky index of GHI ($kc$), the clear-sky index of DNI ($kcb$) can be defined by:

$$kcb = \mathrm{DNI}/\mathrm{DNI}_{\mathrm{cs}}, \tag{7}$$

where $\mathrm{DNI}_{\mathrm{cs}}$ [W/m$^2$] is the clear-sky DNI expectation of REST2 that is available in NSRDB. Apart from clear-sky index ($kc$ and $kcb$), clearness index can also be used to normalize the irradiance measurements [47]. Unlike the clearness index of GHI ($kt$) that is a ratio between the

GHI measurement and the horizontal projection of extraterrestrial solar irradiance ($E_0$), the clearness index of DNI ($ktb$) is calculated by:

$$ktb = \mathrm{DNI}/E_0, \tag{8}$$

where $E_0$ [W/m$^2$] is the extraterrestrial solar irradiance [48].

Although there are different values for solar constant ($E_{sc}$) and equations for $E_0$, for example, the currently accepted value of $E_{sc}$ is 1361 W/m$^2$ [49], the calculation in this work follows the documentation ($E_{sc}$ = 1366.10 W/m$^2$) in PVLIB [50]. Note that the diurnal variation of $E_0$ is not considered as the difference is negligible. The main difference between clear-sky index and clearness index is that clear-sky index takes the air mass and effect of other atmospheric compositions (e.g., aerosol and water vapor) into account, thus the attenuation on solar radiation is dominated by clouds; while clearness index considers all effects from the atmosphere relative to the extraterrestrial irradiance.

### 3.2. Normalization of satellite data

Similarly, the diurnal effects of satellite data should be removed for the benefit of model training, as suggested in [1,8,27]. There are many methods have been proposed for normalizing satellite data and applied for solar irradiance modeling. Satellite measurements can be converted to cloud index [51], reflectance (for reflective bands) [45], and brightness temperature (for emissive bands) [39]. Some standard normalization methods such as Min–Max and Z-score can also be used to normalize the satellite data. Min–Max normalization takes the form:

$$\tilde{L_k} = \frac{L_k - \min(L)}{\max(L) - \min(L)}, \tag{9}$$

where $\tilde{L_k}$ is the $k$th normalized value of $L$, while $\min(L)$ and $\max(L)$ denote the minimum and maximum values in the entire dataset. Therefore, the normalized value of $\tilde{L_k}$ is in the range of [0,1]. Z-score normalization, also called standardization, is in the form of:

$$\tilde{L_k} = (L_k - \mu(L))/\sigma(L), \tag{10}$$

where $\mu(L)$ and $\sigma(L)$ are the mean and standard deviation of the entire dataset $L$, respectively. Then, the normalized $\tilde{L}$ has a mean of 0 and standard deviation of 1. There are also other methods for normalizing satellite data, such as the use of cloud index [6]. For a more detailed description on pre-processing satellite data for solar irradiance modeling, the reader is referred to [1].

There are eight ABI channels (denoted as $b$) used (see Table 2) for deep learning based satellite-to-DNI, and the inputs are spectral satellite images rather than single pixels. The image normalization method proposed in [27] is adopted in this work, since it can remove the diurnal effect and weight each ABI band image equally for cloud detection with convolutional neural networks (CNNs) [27]. For each ABI channel $b$, the minimum ($L^b_{\min}$) and maximum ($L^b_{\max}$) value can be represented, respectively. The minimum and maximum values of each channel can be calculated using the valid range, scale factor, and add offset as shown in Table 2, and more details are available in [39]. The method for normalizing pixels in spectral satellite images can be expressed as:

$$\tilde{L}^b_{ij}|_t = 1 - \frac{L^b_{ij}|_t - L^b_{\min}}{\cos(\theta|_t)(L^b_{\max} - L^b_{\min})}, \tag{11}$$

where $\tilde{L}^b_{ij}|_t$ is the normalized pixel value situated at the $i$th row and $j$th column in the spectral image of band $b$ at time $t$, $L^b_{ij}|_t$ denotes the measured radiance of that pixel, and $\theta|_t$ represents the SZA at time $t$. Some sample normalized spectral images of GOES-16 are shown in Fig. 3.

**Table 3**
Hyperparameters shown in Fig. 4 for Bayesian optimization using the KerasTuner.

| Hyperparameter | Values |
|---|---|
| Optimizer | Adam |
| Loss function | Huber[a] ($\delta$ = 1.0) |
| Learning rate | [1e−5, 1e−4, 2e−4, 5e−4, 1e−3, 2e−3] |
| $x_1$ | range(min = 16, max = 128, step = 2) |
| $a_1$, $a_2$, $a_3$, $a_4$ | [relu, gelu, selu, tanh] |
| $x_2$, $x_3$, $x_4$, $x_5$ | range(min = 8, max = 64, step = 2) |
| $a_5$ | [relu, gelu, selu, linear] |
| Early Stopping | With the patience equal to 5 |

[a] Huber loss is less sensitive to outliers. $\delta$ defines the point where the Huber loss function becomes linear from a quadratic.

### 3.3. Deep learning model for DNI estimation

Due to the spatio-temporal nature of solar irradiance, it is more beneficial to use grid satellite data in satellite-to-irradiance estimation with deep learning [2,40]. Similarly, all satellite bands that can be used for inferring atmosphere characteristics should be included in the inputs of the deep learning satellite-to-DNI model [38,45]. However, there are some GOES-16 bands highly correlated, and such redundant features should be removed in machine learning applications to improve the modeling efficiency [8]. Therefore, inputs used for DNI estimations are spectral satellite images as described in Section 2.2. Since CNNs are specialized in processing structured grid-like data (e.g., satellite images) and have shown superior performance to other machine learning models in satellite-based irradiance estimation [40], CNNs are used as the primary deep learning algorithm in extracting features from spectral satellite images. Given that this work aims to investigate the effectiveness of clearness index in satellite-based DNI estimation with deep learning methods rather than to develop any advanced data-driven models, the model used follows a framework similar to that of [8]. The deep learning model employs CNNs, attention layer, and fully connected dense networks as presented in Fig. 4(a). In the framework, CNNs are to provide specialized neural networks to extract features from satellite images via convolution and pooling with reduced amount of parameters. As feed-forward neural networks designed to deal with data with a grid-structured topology, CNNs are computationally efficient in implementation and hyperparameters tuning [52]. As shown in Fig. 4(b), the convolutional layer is to extract spatial features from the input:

$$y_k = f(w_k * x), \tag{12}$$

where $y_k$ and $w_k$ denote the extracted feature and trainable weights of the $k$th kernel, $x$ is the input, $*$ is the convolution operator, and $f$ represents a nonlinear activation function, where Rectified Linear Unit (ReLU) is one of the representatives, as defined by:

$$f(x) = \max(0, x). \tag{13}$$

Pooling layers are usually grouped with convolutional layers to modify the output and to reduce the dimension gradually with maximum or average of features over local regions [52]. The MaxPooling that forwards the maximum value over the 2 × 2 rectangular neighborhood is adopted in this work (see Fig. 4(b)). The attention layer (with one attention head) is based on the attention mechanism [53] as illustrated in Fig. 4(c), which can enable the model focus more on the target area and improve the learning performance [54,55]. The attention mechanism is expressed as:

$$\mathrm{Attention}(Q, K, V) = \mathrm{Softmax}(Q \cdot K^T/\sqrt{d_k}) \cdot V, \tag{14}$$

where $Q, K, V$ represent the query, key, and value matrices with the dimension of $d_k$, respectively. While the dense layers are applied to learn the relationships between the extracted features and targets.

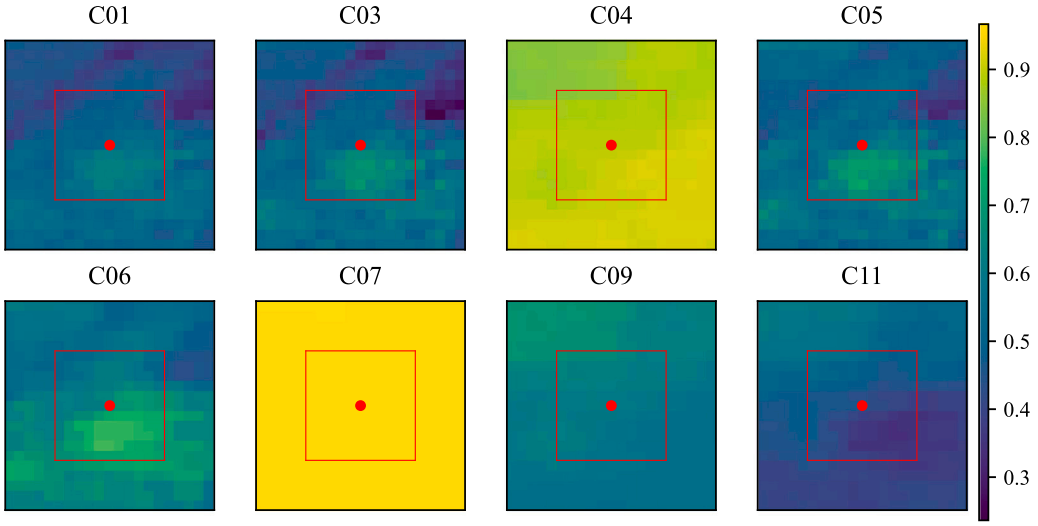


**Fig. 3.** Sample normalized spectral GOES-16 images of the eight selected spectral for Bondville (BON) station (40.05°, −88.37°) at 2020-01-13 18:30:00 (UTC). The whole images are sized of 21 × 21 pixels, where interested region is in the square of 11 × 11 pixels with BON (red point) located at the center. The normalization method is adopted from [27]. (For interpretation of the references to color in this figure legend, the reader is referred to the web version of this article.)

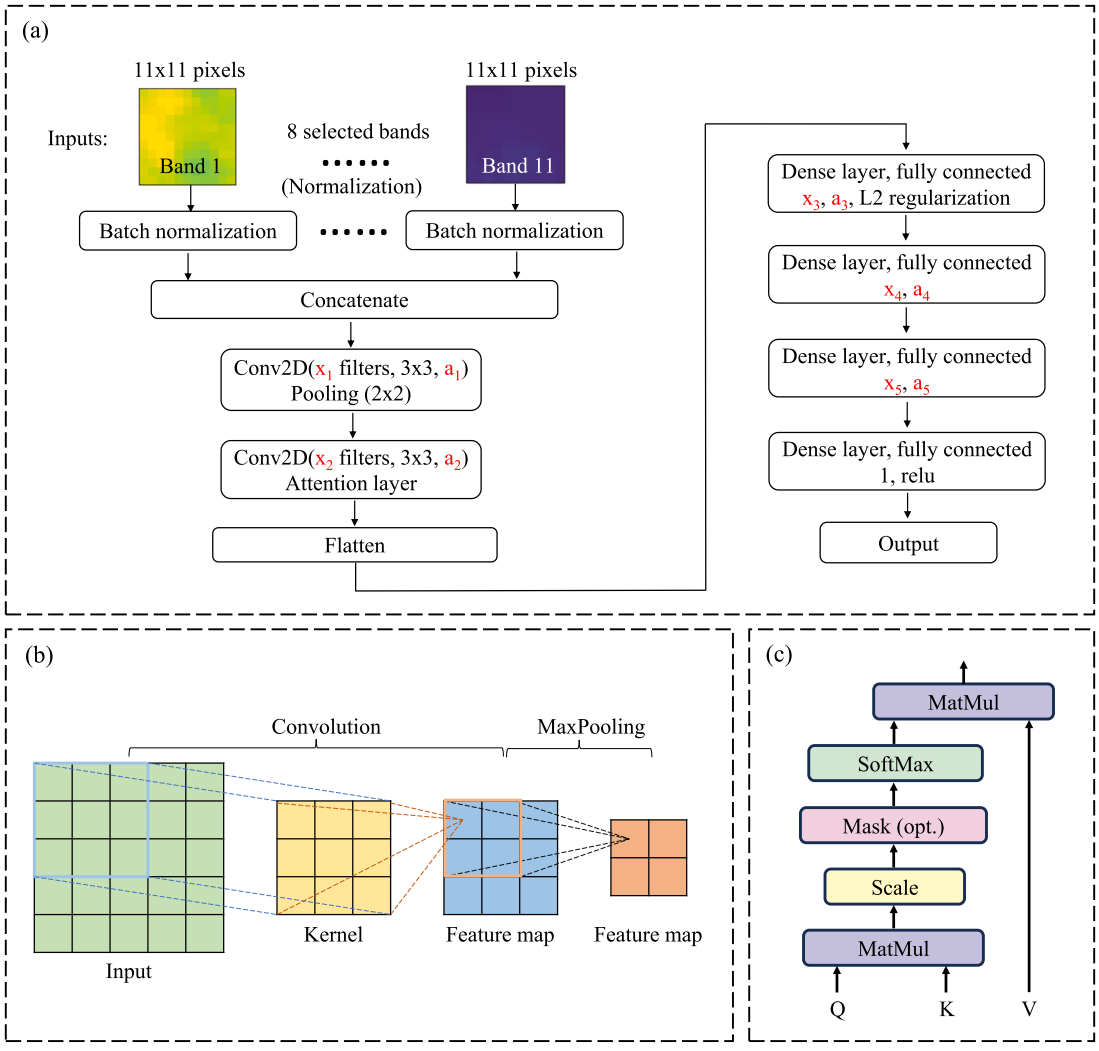


**Fig. 4.** The framework of (a) the deep learning model for DNI estimation from spectral satellite images, where $x_i$ denotes the number of filters, $a_i$ means the activation function, and the output could be clear-sky index or clearness index of DNI. (b) and (c) show the structure of convolutional neural network and attention mechanism used in (a), respectively.

**Table 4**
The RMSE and MBE in [W m$^{-2}$], and nRMSE and nMBE in [%], of 5-min-2-km DNI estimations using deep learning models with normalized satellite data and different outputs: clear-sky index ($kcb$) and clearness index ($ktb$), at all SURFRAD stations. Results on DNI estimation of NSRDB are included as the benchmark, where NSRDB AVG represents the averaged values across the 11 × 11 region same as the used size of used spectral satellite images.

| | RMSE [W m$^{-2}$] (nRMSE [%]) | | | |
|---|---|---|---|---|
| | $kcb$ | $ktb$ | NSRDB | NSRDB AVG |
| BON | **141.76 (22.73)** | 142.20 (22.80) | 165.22 (25.49) | 150.66 (24.21) |
| DRA | 126.54 (15.47) | **122.13 (14.93)** | 146.51 (17.91) | 136.57 (16.69) |
| FPK | **181.50 (29.84)** | 192.23 (31.60) | 206.91 (34.01) | 192.18 (31.59) |
| GWN | 154.77 (25.48) | **152.19 (25.06)** | 209.88 (34.56) | 185.74 (30.65) |
| PSU | **172.58 (30.37)** | 176.12 (30.99) | 219.72 (38.67) | 192.54 (33.84) |
| SXF | **166.39 (26.80)** | 170.04 (27.39) | 217.36 (35.01) | 201.61 (32.46) |
| TBL | 169.00 (24.67) | **167.31 (24.43)** | 205.76 (30.04) | 197.69 (28.82) |
| | MBE [W m$^{-2}$] (nMBE [%]) | | | |
| | $kcb$ | $ktb$ | NSRDB | NSRDB AVG |
| BON | −19.50 (−3.12) | **−16.99 (−2.72)** | 49.74 (7.97) | 41.11 (6.61) |
| DRA | **10.82 (1.32)** | 15.33 (1.87) | 19.17 (2.34) | 20.30 (2.48) |
| FPK | −30.47 (−5.01) | **−1.27 (−0.21)** | 46.64 (7.67) | 42.49 (6.99) |
| GWN | −26.47 (−4.36) | **−12.21 (−2.01)** | 50.69 (8.35) | 43.69 (7.21) |
| PSU | **−0.19 (−0.01)** | −9.90 (−1.74) | 48.20 (8.48) | 38.93 (6.84) |
| SXF | **−26.64 (−4.29)** | −34.91 (−5.62) | 76.57 (12.34) | 58.94 (9.49) |
| TBL | −32.43 (−4.74) | **2.50 (0.36)** | 30.32 (4.43) | 29.81 (4.35) |

Following a similar methodology adopted in [8], cropped spectral satellite images of the eight representative GOES-16 bands are used as inputs for DNI estimation with deep learning. The main difference is that spectral satellite images of the eight selected bands are concatenated before feeding to CNNs in this work, while in [8], spectral images of each band are processed separately and then concatenated. As shown in Fig. 4(a), in satellite-based DNI estimation with deep learning, the spectral satellite images are processed parallelly via batch normalization, then concatenated and fed to convolutional, pooling, and attention layers. Subsequently, the extracted features are flattened as an input vector, which is then used in fully connected dense layers for learning the representation. The L2 regularization applied in dense layers and Early Stopping are used to avoid over-fitting and improve the performance. The output is the clear-sky index or clearness index of DNI as defined in Section 3.1. The DNI clear-sky index and clearness index can be converted back to DNI estimations (with 5-min temporal resolution and 2-km spatial resolution) by multiplying clear-sky DNI expectation of REST2 and extraterrestrial solar irradiance, respectively.

Although deep learning satellite-to-DNI models share the same structure, the hyperparameters could be different for the two outputs (i.e., the clear-sky index and clearness index) and for the seven stations. Therefore, models for each output and for each SURFRAD site are trained separately, and the hyperparameters are tuned using Bayesian optimization of KerasTuner [56] using the settings shown in Table 3. Data in 2019 are used as training (80%) and validation (20%) sets, and data in 2020 are used for testing. The performance evaluation metrics are root mean squared error (RMSE), mean bias error (MBE), their normalized counterparts (nRMSE, nMBE) [8], and the coefficient of determination ($R^2$), as defined by:

$$\mathrm{RMSE} = \sqrt{\frac{1}{N}\sum(e_k - o_k)^2}, \tag{15}$$

$$\mathrm{nRMSE} = \frac{\sqrt{\frac{1}{N}\sum(e_k - o_k)^2}}{\frac{1}{N}\sum o_k}, \tag{16}$$

$$\mathrm{MBE} = \frac{1}{N}\sum(e_k - o_k), \tag{17}$$

$$\mathrm{nMBE} = \frac{\sum(e_k - o_k)}{\sum o_k}, \tag{18}$$

$$R^2 = 1 - \frac{\sum(e_k - o_k)^2}{\sum(e_k - \bar{o_k})^2}, \tag{19}$$

where $e_k$ and $o_k$ are the pair of DNI estimation and ground observation, $\bar{o_k}$ is the mean of observations, $N$ is the total number of compared data points.

## 4. Results and discussion

### 4.1. Comparison between clearness index and clear-sky index with normalized satellite data

As shown in Table 4, compared with DNI estimations of NSRDB, deep learning satellite-to-DNI methods using either clear-sky index or clearness index generally show lower uncertainties in terms of RMSE and MBE. Regardless of the used outputs, deep learning satellite-to-DNI methods show comparatively lower nRMSE in the range of 14.93%–31.60% than NSRDB (17.91%–38.67%). Similarly, the nMBE of deep learning satellite-to-DNI methods shows lower absolute biases (0.01%–5.62%), while DNI estimation in NSRDB has the nMBE range of 2.34%–12.34%. Although averaging NSRDB data across the 11 × 11 region shows improvements (see the comparison between NSRDB and NSRDB AVG), the errors of MBE and RMSE are still higher than those of deep learning models. Generally, the physical satellite-to-DNI method (e.g., NSRDB) overestimates DNI with comparatively higher biases, while deep learning methods show slightly underestimations (see Table 4). This confirms that the DNI estimation in NSRDB should be post-processed with available on-site measurements and deep learning has the potential to reduce uncertainties (e.g., RMSE and MBE) in solar resource assessment with satellite measurements. When comparing the used output for satellite-to-DNI with deep learning, clear-sky index and clearness index generally show comparable performance. In terms of nRMSE, using clear-sky index as the output produces DNI estimation with the nRMSE in the range of 15.47%–30.37%, while using clearness index as the output generates a result with the nRMSE in the range of 14.93%–31.60%. When it comes to the bias, DNI estimation with clear-sky index exhibits slightly lower absolute nMBE values (0.01%–5.01%), while those based on clearness index are in the range of 0.36%–5.62%. This means clearness index can be used as an alternative label in deep learning satellite-to-DNI for improved efficiency.

The scatter plots of DNI estimation-measurement from three methods, namely, the physical method of NSRDB and two deep learning methods based on clear-sky index and clearness index, are presented in Fig. 5. It can be observed that the high-density DNI estimation-measurement points are distributed along with the identity line, which means DNI estimations have a correct time alignment with DNI measurements. The points near the identity line, especially at the range of high DNI measurements, have much higher densities than elsewhere. This indicates that DNI estimations for clear and less cloudy sky conditions have a higher accuracy than those in cloudy and overcast periods.

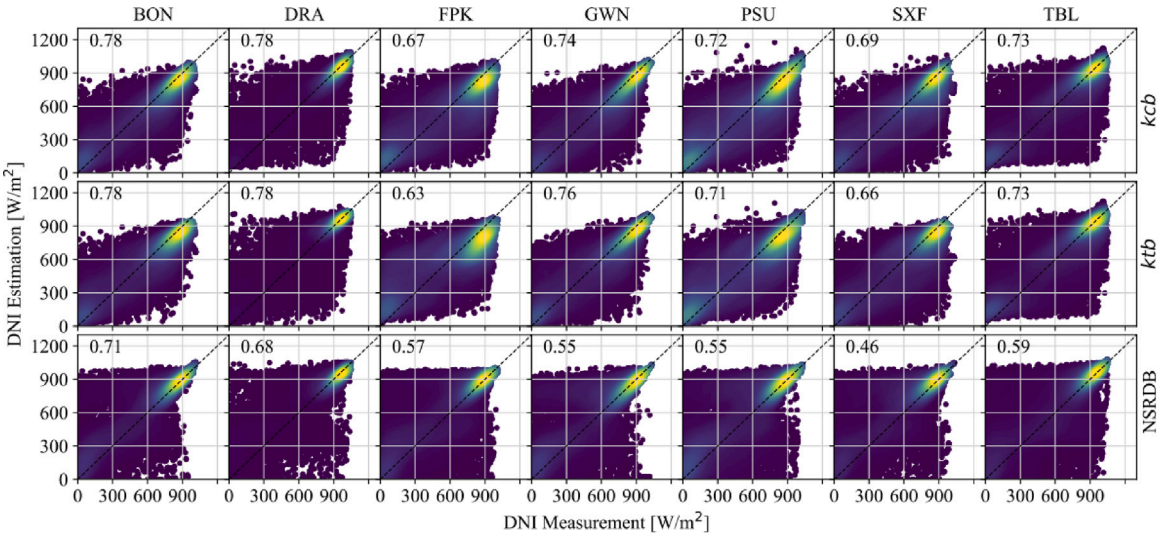


**Fig. 5.** Scatter plots of DNI estimation–measurement pairs, from three satellite-to-DNI methods, namely, physical method of NSRDB and deep learning methods with clear-sky index (*kcb*) and clearness index (*ktb*), at seven SURFRAD stations. The number in each subplot is the coefficient of determination ($R^2$) between DNI estimations and measurements, a higher $R^2$ indicates a better performance.

**Table 5**
The RMSE and MBE in [W m$^{-2}$], and nRMSE and nMBE in [%], of DNI estimations using different deep learning models at SURFRAD stations. "*kcb*" denotes the method using normalized satellite data and clear-sky index, while "*ktb*_UNS" represents the method based on unnormalized satellite data and clearness index.

| | RMSE [W m$^{-2}$] (nRMSE [%]) | | MBE [W m$^{-2}$] (nMBE [%]) | |
|---|---|---|---|---|
| | *kcb* | *ktb*_UNS | *kcb* | *ktb*_UNS |
| BON | 141.76 (22.73) | **136.00 (21.80)** | −19.50 (−3.12) | **0.53 (0.09)** |
| DRA | 126.54 (15.47) | **112.35 (13.73)** | **10.82 (1.32)** | −21.42 (−2.62) |
| FPK | 181.50 (29.84) | **164.13 (26.98)** | −30.47 (−5.01) | **−7.66 (−1.26)** |
| GWN | 154.77 (25.48) | **134.49 (22.15)** | −26.47 (−4.36) | **−6.59 (−1.09)** |
| PSU | 172.58 (30.37) | **159.44 (28.06)** | **−0.19 (−0.01)** | 14.54 (2.56) |
| SXF | 166.39 (26.80) | **147.09 (23.69)** | −26.64 (−4.29) | **−22.84 (−3.68)** |
| TBL | 169.00 (24.67) | **139.41 (20.35)** | −32.43 (−4.74) | **−21.81 (−3.18)** |

The lower $R^2$ values in subplots of Fig. 5 show that DNI estimations in NSRDB have an inferior performance compared with those of deep learning satellite-to-DNI methods. Meanwhile, it can be observed that there are more points of NSRDB distributed above the identity line, which means NSRDB tends to generate high-estimation-low-measurement errors. This overestimation usually leads to positive biases as shown in Table 4. It can be inferred that physical method of NSRDB underestimates the cloud amount using satellite measurements [8] for DNI estimations. Compared with the scatter plots of estimation-measurement for NSRDB, deep learning satellite-to-DNI methods generally do not show obvious over-estimations (points above the diagonal line) or under-estimations (points below the diagonal line). The refined biases and improved $R^2$ values indicate that deep learning can enhance the satellite-to-DNI conversion with better extraction of cloud information from spectral satellite measurements, where the use of clearness index can improve the modeling efficiency.

### 4.2. The role of normalizing satellite data

As mentioned in Section 3.1, the clear-sky index and clearness index for normalizing DNI are based on different calculations, the former employs clear-sky DNI estimation, while the latter uses extraterrestrial solar radiation. As they have different physical meanings in representing attenuation effects of the atmosphere, this section is to discuss how to use satellite data in deep learning satellite-to-DNI methods with different outputs, namely, clear-sky index and clearness index with normalized and unnormalized satellite data, respectively. Note that even spectral satellite measurements are not normalized, the batch normalization layer is still employed in the deep learning model as shown in Fig. 4.

The comparison of two deep learning satellite-to-DNI methods with different inputs and outputs is presented in Table 5. Generally, deep learning method (*ktb*_UNS) based on clearness index and unnormalized satellite data yields DNI estimations with lower uncertainties than the model (*kcb*) using normalized satellite data and clear-sky index. In terms of nRMSE, satellite-to-DNI estimations based on clearness index have the error in the range of 13.73%–28.06%. This is comparatively lower than the nRMSE of DNI estimations based on clear-sky index (15.47%–30.37%), across all seven SURFRAD stations. Meanwhile, the absolute bias of DNI estimations based on clear-sky index is in the range of 0.01%–5.01%, while those of the method using clearness index have the bias of 0.09%–3.68% (absolute value). The nRMSE values of DNI estimations with clearness index are typically lower than those based on clear-sky index at all SURFRAD stations. The reason might be that the errors of REST2 in calculating clear-sky DNI expectation introduce a higher uncertainty in the clear-sky index, which could lead to error accumulations in the DNI estimations. Although there is no obvious trend observed regarding the bias for DNI estimation, the absolute bias of DNI estimation with clearness index is relatively less than those based on the clear-sky index. This demonstrates that clearness index can be used for satellite-based DNI estimation with reduced uncertainties.

To further evaluate the performance of DNI estimations based on the two indexes and NSRDB, the marginal distributions of DNI estimations and measurements are shown in Fig. 6. The number in each subplot represents the Wasserstein distance (also called the optimal transport

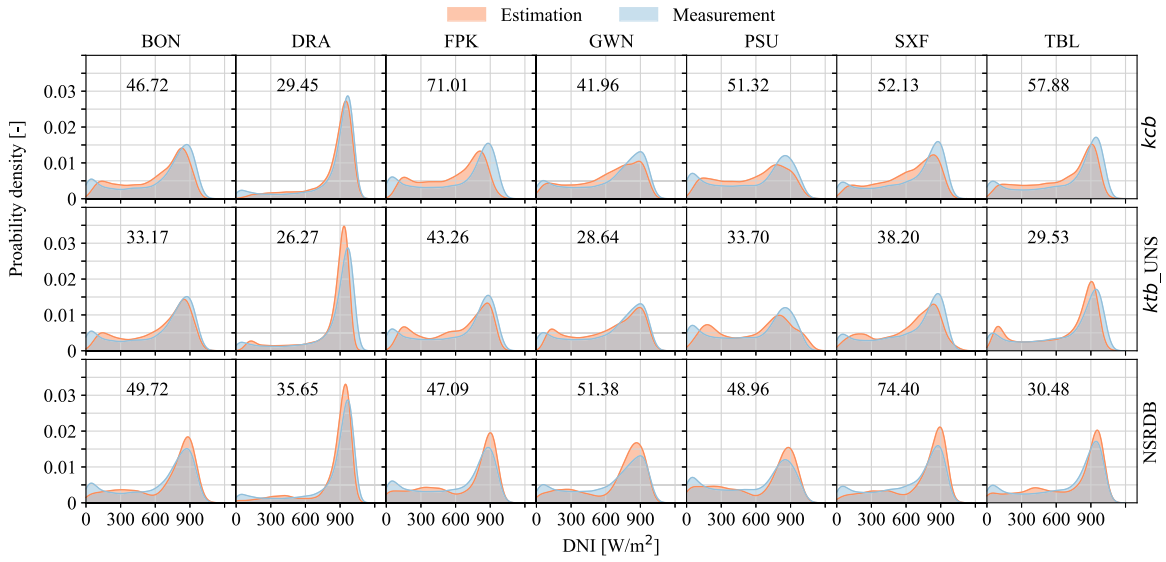


**Fig. 6.** Marginal distributions of DNI estimations and measurements, from two deep learning satellite-to-DNI methods and NSRDB, at seven SURFRAD stations. "*kcb*" denotes the method using normalized satellite data and clear-sky index, while "*ktb*_UNS" represents the method based on unnormalized satellite data and clearness index. The number in each subplot means the Wasserstein distance between two distributions, a smaller Wasserstein distance indicates a higher similarity.

distance) that describes the similarity between two probability distributions. It is then obvious that DNI estimations based on clearness index generally show higher similarity to the measurements than those from clear-sky index and NSRDB. It can also be observed that deep learning satellite-to-DNI methods tend to underestimate DNI at both high- and low-irradiance conditions, while the over-estimation usually occurs at the medium-irradiance condition. As for NSRDB, the over-estimation at high-irradiance conditions and under-estimation at low-irradiance condition are more obvious. DNI estimations from clearness index generally show more agreements with the measurements at all conditions compared with those based on the clear-sky index and NSRDB.

Based on the comparisons presented in Table 5 and Fig. 6, in deep learning based satellite-to-DNI estimation, the use of clearness index generally produces an improved overall result than applying the clear-sky index. This means clearness index can better represent attenuation effects of the atmosphere. Besides the improved performance in satellite-based DNI estimation with deep learning, clearness index can offer two more advantages: (1) clearness index based on extraterrestrial solar radiation is easier to obtain than clear-sky index, as the implementation of a high-accuracy clear-sky model (e.g., REST2) requires much more efforts; (2) The normalization of spectral satellite data is not required in deep learning satellite-to-DNI methods with clearness index, which saves a lot of time and computing resources in data pre-processing. These advantages on accuracy and efficiency are more obvious for satellite-to-DNI estimation with deep learning for regional or national satellite-to-irradiance applications.

### 4.3. Further comparison and error analysis

Since clouds are the main factor attenuating solar radiation on the ground level, further comparisons of DNI estimations using clear-sky index (*kcb* with normalized satellite data) and clearness index (*ktb*_UNS with unnormalized satellite data) under different sky conditions are presented in this section. Sky conditions are classified using the Bright-Sun clear-sky detection algorithm with 1-min data [57], where a 5-min period is marked clear-sky only if all 1-min data points within it are detected as clear; otherwise, it is classified as cloudy. Note that cloudy is different from overcast (when DNI should be zero), and specific cloud types are not classified but generally grouped as cloudy (the percentages of cloudy periods at SURFRAD stations are in the range of 50.12%–85.36% [29]). This is different from the method used in [58] with cloud fractions. Table 6 shows the result of DNI estimations with two deep learning satellite-to-DNI methods (*kcb* and *ktb*_UNS) and NSRDB, under cloudy and clear sky conditions. It can be observed that DNI estimations under cloudy skies are generally associated with larger uncertainties than those of clear periods. NSRDB tends to have overall lower errors under clear skies due to the use of REST2 clear-sky model. However, there are also some cases when DNI estimations have larger divergences (see the RMSE/nRMSE values at FPK and PSU for deep learning based methods, and GWN and SXF for NSRDB, in Table 6). The possible reason is that DNI is more sensitive to the atmospheric compositions (e.g., aerosol and water vapor under clear skies) than GHI, the retrieval of DNI from satellite measurements faces more challenges and thus are with higher discrepancies. This has also been observed in other physical, empirical, or data-driven methods for DNI estimations under clear sky conditions [8,34]. Although clouds are known as the primary factor affecting solar radiation and many studies have been conducted on cloud detection from satellite images, the retrieval of other atmospheric constitutes, namely, aerosol and water vapor, is also crucial for satellite-to-DNI estimations.

When comparing deep learning satellite-to-DNI methods with the two indexes, although there are some site-specific differences under clear-sky conditions, DNI estimations based on clear-sky index generally show larger nRMSE values (4.03%–15.42%) than those based on clearness index (4.02%–14.41%). The reason could that the used spectral satellite bands may not be able to effectively capture the information on aerosols and water vapor in clear-sky conditions. Moreover, DNI estimations based on clearness index typically have lower biases with the absolute nMBE in the range of 0.67%–5.79%, while the absolute biases of DNI estimations using clear-sky index ranges 1.21%–10.29%. When it comes to cloudy conditions, NSRDB generally show higher uncertainties for RMSE and MBE, while DNI estimations based on clearness index have reduced nRMSE in the range of 23.83%–34.06%, which are comparatively lower than those from clear-sky index (27.31%–36.97%). DNI estimations based on clearness index also tend to have lower biases with the absolute nMBE of 0.28%–3.48% than those with clear-sky index (0.90%–4.10%). Although using clearness index in satellite-to-DNI estimation may result in some slightly enlarged errors in clear sky conditions as shown in Table 6, clearness index is still an promising alternative target in deep learning satellite-to-DNI estimations, with the potential to reduce the uncertainties for

**Table 6**
The RMSE and MBE in [W m$^{-2}$], and nRMSE and nMBE in [%], of DNI estimation using different deep learning models at SURFRAD stations under clear and cloudy conditions. "*kcb*" denotes the method using normalized satellite data and clear-sky index, while "*ktb*_UNS" represents the method based on unnormalized satellite data and clearness index.

| Sky condition | Station | RMSE [W m$^{-2}$] (nRMSE [%]) | | | MBE [W m$^{-2}$] (nMBE [%]) | | |
|---|---|---|---|---|---|---|---|
| | | *kcb* | *ktb*_UNS | NSRDB | *kcb* | *ktb*_UNS | NSRDB |
| Clear | BON | 68.55 (7.99) | 84.87 (9.89) | **37.08 (4.32)** | −36.78 (−4.28) | −14.76 (−1.72) | **12.94 (1.51)** |
| | DRA | **38.30 (4.03)** | 42.07 (4.42) | 39.44 (4.15) | **−11.53 (−1.21)** | −25.00 (−2.63) | −18.93 (−1.99) |
| | FPK | 134.64 (15.42) | 125.82 (14.41) | **58.68 (6.72)** | −89.86 (−10.29) | −50.58 (−5.79) | **2.25 (0.26)** |
| | GWN | 47.06 (5.32) | **35.59 (4.02)** | 122.44 (13.85) | −32.13 (−3.63) | **−5.90 (−0.67)** | −28.90 (−3.27) |
| | PSU | 53.81 (6.09) | 57.71 (6.53) | **50.33 (5.70)** | −23.34 (−2.64) | 14.10 (1.60) | **−4.33 (−0.49)** |
| | SXF | 102.35 (12.00) | **83.75 (9.82)** | 109.66 (12.86) | −52.24 (−6.13) | −32.23 (−3.78) | **−0.45 (−0.05)** |
| | TBL | 90.59 (9.79) | **54.82 (5.93)** | 71.14 (7.69) | −52.36 (−5.66) | −25.48 (−2.75) | **−0.32 (−0.03)** |
| Cloudy | BON | 157.53 (28.27) | **148.26 (26.61)** | 187.57 (33.66) | −14.61 (−2.62) | **5.44 (0.98)** | 60.62 (10.88) |
| | DRA | 178.16 (27.31) | **155.31 (23.83)** | 215.23 (33.00) | 20.79 (3.19) | **1.85 (0.28)** | 66.78 (10.24) |
| | FPK | 191.95 (35.64) | **172.82 (32.09)** | 230.63 (42.83) | −14.75 (−2.74) | **3.71 (0.69)** | 58.38 (10.84) |
| | GWN | 178.66 (33.58) | **156.08 (29.33)** | 232.82 (43.76) | −22.64 (−4.26) | **−8.54 (−1.61)** | 76.85 (14.44) |
| | PSU | 187.50 (36.97) | **172.72 (34.06)** | 239.57 (47.24) | **4.56 (0.90)** | 14.63 (2.88) | 58.51 (11.54) |
| | SXF | 185.20 (33.66) | **164.73 (29.94)** | 242.19 (44.01) | **−17.93 (−3.26)** | −18.15 (−3.30) | 102.00 (18.54) |
| | TBL | 193.07 (33.12) | **162.70 (27.91)** | 241.39 (41.40) | −23.90 (−4.10) | **−20.30 (−3.48)** | 43.33 (7.43) |

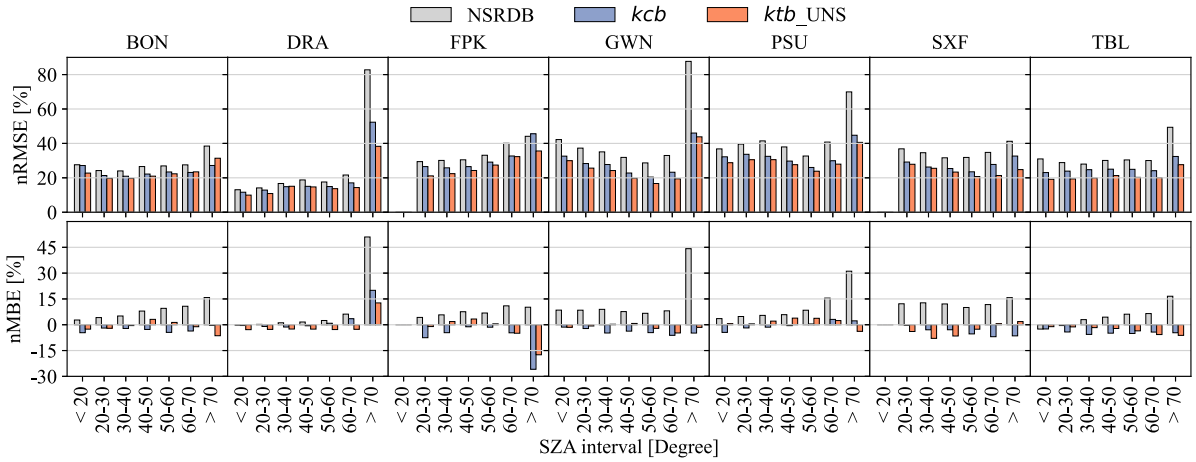


**Fig. 7.** The nRMSE [%] and nMBE [%] of DNI estimations, from two deep learning satellite-to-DNI methods and NSRDB, in different intervals of solar zenith angle (SZA), at seven SURFRAD stations. "*kcb*" denotes the method using normalized satellite data and clear-sky index, while "*ktb*_UNS" represents the method based on unnormalized satellite data and clearness index.

all-sky DNI estimations. However, future studies on how to use clearness index in satellite-to-DNI estimation with deep learning under clear-sky conditions should be conducted to improve the accuracy.

The nRMSE and nMBE of DNI estimations in different intervals of SZA with the two methods (*kcb* and *ktb*_UNS) and NSRDB are presented in Fig. 7 to further evaluate their performance. It is shown that DNI estimations of NSRDB show comparatively larger errors of nRMSE and nMBE across all SZA intervals. DNI estimations based on clearness index generally have lower nRMSE values than those with clear-sky index across different intervals of SZA at all SURFRAD stations. Overall, DNI estimations with clearness index tend to have relatively smaller biases. As mentioned in Section 3.1, the SZA is corresponded to the air mass that describes the direct optical path through the atmosphere (a higher SZA indicates a larger air mass). The lower discrepancies of DNI estimations in different intervals of SZA may indicate that clearness index with unnormalized satellite data could better account for the attenuation on DNI when passing through the atmosphere at different optical lengths. Since modern geostationary satellites are equipped with more advanced sensors with increased spectral responses and spatio-temporal resolutions, the multi-spectral satellite measurements could be used in data-driven satellite-to-DNI estimations to better extract the information on atmospheric compositions. This is not limited to clouds but also includes water vapor, aerosols, and other components, where the clearness index may be a better indicator to represent the optical path that DNI passes through in the atmosphere.

### 4.4. Generic applicability of the proposed method

The use of clearness index in satellite-to-DNI estimation with deep learning shows promising results when the model is trained and tested using data from the station of interest itself. This section is to explore the generic applicability of the proposed method across different stations, where the models are trained with data from several selected locations and then applied to other sites that are not involved with the model training. Since the seven SURFRAD stations are distributed in different climate zones as shown in Fig. 1, only using data from one station to train the model might have a poor performance at other locations, especially for locations with different climate characteristics [16,46]. Therefore, the transferred models in this section are trained using data from five stations, and then applied at two excluded stations for DNI estimations in 2020. There are four stations in total involved in this evaluation, namely, SXF and TBL (the model is trained using data from BON, DRA, FPK, GWN, and PSU), and FPK and GWN (the model is developed with data from BON, DRA, PSU, SXF, and TBL).

The overall results of the two transferred models, namely, one based on clear-sky-index and normalized satellite data (*kcb*_T) and the other based on clearness index and unnormalized data (*ktb*_UNST), are shown in Fig. 8. Compared with the locally trained model of *ktb*_UNST, transferred methods have relatively higher nRMSE values, but still less than those of NSRDB. For the decreased nRMSE of transferred methods compared with *kcb* at FPK, GWN, and SXF, the possible reason

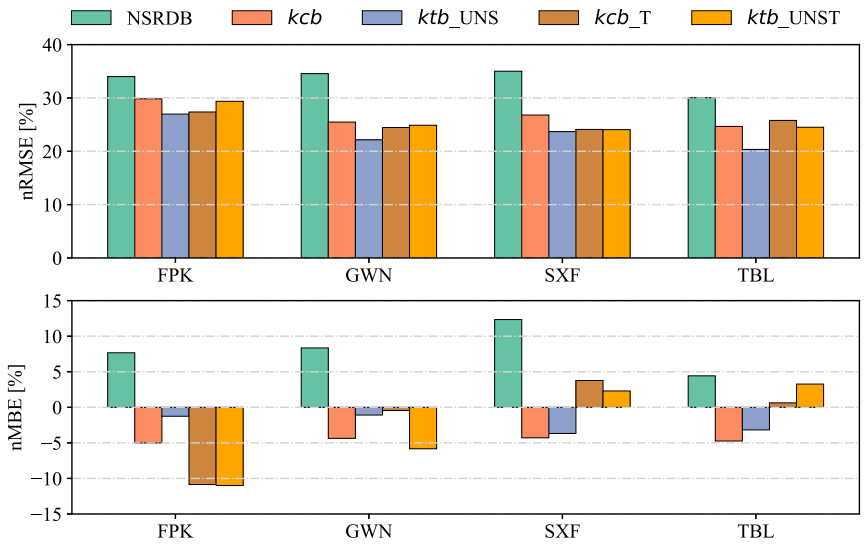


**Fig. 8.** Comparison of the nRMSE [%] and nMBE [%] of DNI estimations in 2020, from different methods, at stations of Fort Peck (FPK), Goodwin Creek (GWN), Sioux Falls (SXF), and Table Mountain (TBL). "*kcb*" denotes the method using normalized satellite data and clear-sky index, while "*ktb*_UNS" represents the method based on unnormalized satellite data and clearness index. "*kcb*_T" and "*ktb*_UNST" are the methods trained without using data from SXF and TBL based on "*kcb*" and "*ktb*_UNS", respectively.

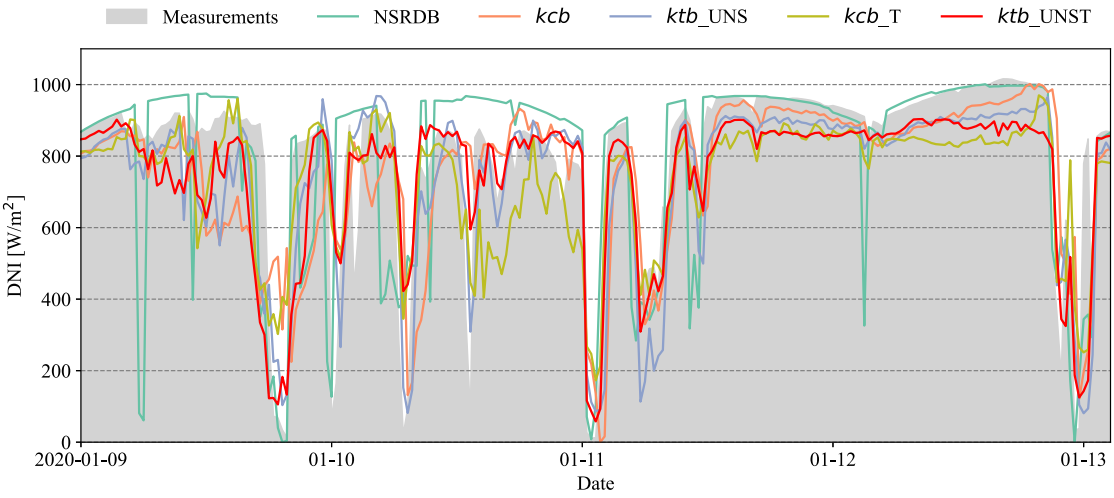


**Fig. 9.** A time series comparison of DNI measurements and estimations from different methods at Table Mountain (TBL) station, where nighttime periods are excluded. "*kcb*" denotes the method using normalized satellite data and clear-sky index, while "*ktb*_UNS" represents the method based on unnormalized satellite data and clearness index. "*kcb*_T" and "*ktb*_UNST" are the methods trained without using data from SXF and TBL based on "*kcb*" and "*ktb*_UNS", respectively.

could be the benefit from data of multiple locations for representation learning. NSRDB also show overall larger biases than the transferred models (see Fig. 8). In addition, a sample time series comparison of DNI measurements and estimations from different methods at TBL are presented in Fig. 9. It can be observed that NSRBD sometimes exhibits comparatively larger deviations, while others can capture the fluctuations of the DNI measurements but are also associated with varying uncertainties. Nevertheless, clearness index can be used as a better target in deep learning based satellite-to-DNI estimation for both local and transferred applications, which can enhance the modeling accuracy and efficiency. This is even more beneficial for regional applications.

## 5. Conclusions

Owing to the scarcity of in-situ irradiance measurements, satellite-derived irradiance usually serves as one of the alternative data sources in solar resource assessment. Nonetheless, satellite-derived irradiance of DNI shows high uncertainties. As DNI is also an indispensable part in solar energy applications, this work aims to improve 5-min satellite-based DNI estimation with clearness index and deep learning methods. Compared with physical methods, deep learning is likely to yield better overall DNI estimations with satellite data. Results also show that clearness index can be used as the target in deep learning models to produce comparable 5-min satellite-based DNI estimations with the clear-sky index. This provides additional benefits in satellite-based DNI estimations, as clearness index can be easily calculated, while clear-sky index usually requires extra efforts in implementing the clear-sky model.

Clearness index and Clear-sky index of DNI account for the attenuation effects of atmospheric compositions in different ways, the former considers the direct optical path that DNI passes through while the latter is more focused on the cloud. This indicates that the pre-processing methods of satellite data should be different. It is found that clearness index based DNI estimation with unnormalized satellite inputs tend to have better performance than those based on clear-sky index and normalized satellite data. The reason might be that clearness index and unnormalized satellite data could better reflect

the interactions between DNI and the atmosphere. With unnormalized satellite data, clearness index based DNI estimation can further improve the efficiency in regional 5-min satellite-to-DNI conversions.

Under the evaluation of different sky conditions, satellite-based DNI estimations with deep learning tend to underestimate DNI at both high- and low-irradiance conditions and clouds are still the root cause of large errors. DNI estimations with clearness index sometimes also face enlarged errors in clear-sky conditions. These sources of larger discrepancies indicate that more efforts are still needed in better extracting cloud and other atmospheric information from spectral satellite images and representing the long optical path that DNI travels through at high SZAs. Nevertheless, the use of clearness index in satellite-based DNI estimation with deep learning provides an alternative to improve the accuracy and efficiency, which is also applicable for transferred applications where ground-based training data is not available. Apart from the improved performance, satellite-to-DNI with clearness index offers additional advantages on data pre-processing and computing resources, which is more beneficial for large-scale applications.

## CRediT authorship contribution statement

**Shanlin Chen:** Writing – original draft, Validation, Methodology, Investigation, Conceptualization. **Tao Jing:** Writing – review & editing, Validation, Investigation. **Mengying Li:** Writing – review & editing, Validation, Supervision, Investigation. **Hiu Hung Lee:** Writing – review & editing, Validation, Supervision, Project administration. **Siqi Bu:** Writing – review & editing, Validation, Supervision, Project administration, Funding acquisition.

## Declaration of competing interest

The authors declare that they have no known competing financial interests or personal relationships that could have appeared to influence the work reported in this paper.

## Acknowledgments

This study was supported by the Centre for Advances in Reliability and Safety (CAiRS) and funded in part by the InnoHK initiative of the Innovation and Technology Commission of the Hong Kong Special Administrative Region Government.

## Data availability

The data used in this work are publicly available. SURFRAD measurements are available at https://gml.noaa.gov/aftp/data/radiation/surfrad/, satellite data of GOES-16 can be accessed at https://noaa-goes16.s3.amazonaws.com/index.html, and NSRDB data are accessible via https://nsrdb.nrel.gov/data-viewer.

## References

[1] Y. Chu, Y. Wang, D. Yang, S. Chen, M. Li, A review of distributed solar forecasting with remote sensing and deep learning, Renew. Sustain. Energy Rev. 198 (2024) 114391.
[2] D. Yang, W. Wang, C.A. Gueymard, T. Hong, J. Kleissl, J. Huang, M.J. Perez, R. Perez, J.M. Bright, X. Xia, D. van der Meer, I.M. Peters, A review of solar forecasting, its dependence on atmospheric sciences and implications for grid integration: Towards carbon neutrality, Renew. Sustain. Energy Rev. 161 (2022) 112348.
[3] IEA, Renewables 2024 [online], 2024, Available at: https://www.iea.org/reports/renewables-2024. (Accessed 31 October 2024).
[4] J. Kleissl, Solar Energy Forecasting and Resource Assessment, Academic Press, 2013.
[5] D. Yang, W. Wang, X. Xia, A concise overview on solar resource assessment and forecasting, Adv. Atmospheric Sci. (2022) 1–13.
[6] S. Chen, Z. Liang, S. Guo, M. Li, Estimation of high-resolution solar irradiance data using optimized semi-empirical satellite method and GOES-16 imagery, Sol. Energy 241 (2022) 404–415.
[7] G. Huang, Z. Li, X. Li, S. Liang, K. Yang, D. Wang, Y. Zhang, Estimating surface solar irradiance from satellites: Past, present, and future perspectives, Remote Sens. Environ. 233 (2019) 111371.
[8] S. Chen, C. Li, Y. Xie, M. Li, Global and direct solar irradiance estimation using deep learning and selected spectral satellite images, Appl. Energy 352 (2023) 121979.
[9] M. Sengupta, Y. Xie, A. Lopez, A. Habte, G. Maclaurin, J. Shelby, The National Solar Radiation Database (NSRDB), Renew. Sustain. Energy Rev. 89 (2018) 51–60.
[10] G. Buster, M. Bannister, A. Habte, D. Hettinger, G. Maclaurin, M. Rossol, M. Sengupta, Y. Xie, Physics-guided machine learning for improved accuracy of the National Solar Radiation Database, Sol. Energy 232 (2022) 483–492.
[11] Y. Xie, M. Sengupta, J. Yang, G. Buster, B. Benton, A. Habte, Y. Liu, Integration of a physics-based direct normal irradiance (DNI) model to enhance the National Solar Radiation Database (NSRDB), Sol. Energy 266 (2023) 112195.
[12] M. Sengupta, A. Habte, S. Wilbert, C. Gueymard, J. Remund, Best Practices Handbook for the Collection and Use of Solar Resource Data for Solar Energy Applications, Technical Report, National Renewable Energy Lab. (NREL), Golden, CO (United States), 2021.
[13] W. Greuell, J. Meirink, P. Wang, Retrieval and validation of global, direct, and diffuse irradiance derived from SEVIRI satellite observations, J. Geophys. Res.: Atmospheres 118 (5) (2013) 2340–2361.
[14] Z. Qu, A. Oumbe, P. Blanc, B. Espinar, G. Gesell, B. Gschwind, L. Klüser, M. Lefèvre, L. Saboret, M. Schroedter-Homscheidt, et al., Fast radiative transfer parameterisation for assessing the surface solar irradiance: The Heliosat-4 method, Meteorol. Z. 26 (1) (2017) 33–57.
[15] J.-Y. Han, P. Vohnicky, Estimation of global and diffuse horizontal irradiance by machine learning techniques based on variables from the Heliosat model, J. Clean. Prod. 371 (2022) 133696.
[16] H. Shi, D. Yang, W. Wang, D. Fu, L. Gao, J. Zhang, B. Hu, Y. Shan, Y. Zhang, Y. Bian, et al., First estimation of high-resolution solar photovoltaic resource maps over China with Fengyun-4A satellite and machine learning, Renew. Sustain. Energy Rev. 184 (2023) 113549.
[17] D. Yang, Validation of the 5-min irradiance from the National Solar Radiation Database (NSRDB), J. Renew. Sustain. Energy 13 (1) (2021) 016101.
[18] Y. Chu, D. Yang, H. Yu, X. Zhao, M. Li, Can end-to-end data-driven models outperform traditional semi-physical models in separating 1-min irradiance? Appl. Energy 356 (2024) 122434.
[19] D. Yang, Solar radiation on inclined surfaces: Corrections and benchmarks, Sol. Energy 136 (2016) 288–302.
[20] A. Laguarda, R. Alonso-Suárez, G. Abal, Improved estimation of hourly direct normal solar irradiation (DNI) using geostationary satellite visible channel images over moderate albedo areas, Sol. Energy 259 (2023) 30–40.
[21] A.C.S. Porfirio, J.C. Ceballos, A method for estimating direct normal irradiation from GOES geostationary satellite imagery: Validation and application over Northeast Brazil, Sol. Energy 155 (2017) 178–190.
[22] C.A. Gueymard, REST2: High-performance solar radiation model for cloudless-sky irradiance, illuminance, and photosynthetically active radiation–Validation with a benchmark dataset, Sol. Energy 82 (3) (2008) 272–285.
[23] M. Lefèvre, A. Oumbe, P. Blanc, B. Espinar, B. Gschwind, Z. Qu, L. Wald, M. Schroedter-Homscheidt, C. Hoyer-Klick, A. Arola, et al., McClear: a new model estimating downwelling solar radiation at ground level in clear-sky conditions, Atmospheric Meas. Tech. 6 (9) (2013) 2403–2418.
[24] R.A. Ramadhan, Y.R. Heatubun, S.F. Tan, H.-J. Lee, Comparison of physical and machine learning models for estimating solar irradiance and photovoltaic power, Renew. Energy 178 (2021) 1006–1019.
[25] J. Wu, J. Niu, Q. Qi, C.A. Gueymard, L. Wang, W. Qin, Z. Zhou, Reconstructing 10-km-resolution direct normal irradiance dataset through a hybrid algorithm, Renew. Sustain. Energy Rev. 204 (2024) 114805.
[26] T. Jing, S. Chen, D. Navarro-Alarcon, Y. Chu, M. Li, SolarFusionNet: Enhanced solar irradiance forecasting via automated multi-modal feature selection and cross-modal fusion, IEEE Trans. Sustain. Energy (2024).
[27] L.M. Matsunobu, H.T.C. Pedro, C.F.M. Coimbra, Cloud detection using convolutional neural networks on remote sensing images, Sol. Energy 230 (2021) 1020–1032.
[28] Q. Paletta, G. Terrén-Serrano, Y. Nie, B. Li, J. Bieker, W. Zhang, L. Dubus, S. Dev, C. Feng, Advances in solar forecasting: Computer vision with deep learning, Adv. Appl. Energy (2023) 100150.
[29] S. Chen, C. Li, R. Stull, M. Li, Improved satellite-based intra-day solar forecasting with a chain of deep learning models, Energy Convers. Manage. 313 (2024) 118598.
[30] F. Antonanzas-Torres, R. Urraca, J. Polo, O. Perpiñán-Lamigueiro, R. Escobar, Clear sky solar irradiance models: A review of seventy models, Renew. Sustain. Energy Rev. 107 (2019) 374–387.
[31] J.A. Augustine, J.J. DeLuisi, C.N. Long, SURFRAD–A national surface radiation budget network for atmospheric research, Bull. Am. Meteorol. Soc. 81 (10) (2000) 2341–2358.
[32] D. Yang, SolarData: An R package for easy access of publicly available solar datasets, Sol. Energy 171 (2018) A3–A12.

[33] C.N. Long, Y. Shi, An automated quality assessment and control algorithm for surface radiation measurements, Open Atmospheric Sci. J. 2 (1) (2008).
[34] S. Chen, M. Li, Improved turbidity estimation from local meteorological data for solar resourcing and forecasting applications, Renew. Energy 189 (2022) 259–272.
[35] D. Yang, W. Wang, J.M. Bright, C. Voyant, G. Notton, G. Zhang, C. Lyu, Verifying operational intra-day solar forecasts from ECMWF and NOAA, Sol. Energy 236 (2022) 743–755.
[36] G. Zhang, D. Yang, G. Galanis, E. Androulakis, Solar forecasting with hourly updated numerical weather prediction, Renew. Sustain. Energy Rev. 154 (2022) 111768.
[37] H.E. Beck, T.R. McVicar, N. Vergopolan, A. Berg, N.J. Lutsko, A. Dufour, Z. Zeng, X. Jiang, A.I. van Dijk, D.G. Miralles, High-resolution (1 km) Köppen–Geiger maps for 1901–2099 based on constrained CMIP6 projections, Sci. Data 10 (1) (2023) 724.
[38] T.J. Schmit, S.S. Lindstrom, J.J. Gerth, M.M. Gunshor, Applications of the 16 spectral bands on the advanced baseline imager (ABI), 2018.
[39] Goes R series product definition and users' guide (pug) volume 3: Level 1B products, 2019, Available at: https://www.goes-r.gov/users/docs/PUG-L1b-vol3.pdf.
[40] H. Jiang, N. Lu, G. Huang, L. Yao, J. Qin, H. Liu, Spatial scale effects on retrieval accuracy of surface solar radiation using satellite data, Appl. Energy 270 (2020) 115178.
[41] Z. Liao, C.F. Coimbra, Hybrid solar irradiance nowcasting and forecasting with the SCOPE method and convolutional neural networks, Renew. Energy 232 (2024) 121055.
[42] Y. Xie, M. Sengupta, Y. Liu, H. Long, Q. Min, W. Liu, A. Habte, A physics-based DNI model assessing all-sky circumsolar radiation, IScience 23 (3) (2020).
[43] M. Sengupta, Y.-K. Xie, A. Habte, B.N. Benton, P. Edwards, G. Maclaurin, M.J. Foster, A. Heidinger, Improving the national solar radiation data base using PSM v4, in: 105th Annual AMS Meeting 2025, vol. 105, 2025, 455074.
[44] D. Yang, Choice of clear-sky model in solar forecasting, J. Renew. Sustain. Energy 12 (2) (2020) 026101.
[45] H. Jiang, N. Lu, J. Qin, W. Tang, L. Yao, A deep learning algorithm to estimate hourly global solar radiation from geostationary satellite data, Renew. Sustain. Energy Rev. 114 (2019) 109327.
[46] S. Chen, Z. Liang, P. Dong, S. Guo, M. Li, A transferable turbidity estimation method for estimating clear-sky solar irradiance, Renew. Energy 206 (2023) 635–644.
[47] P. Lauret, R. Alonso-Suárez, J. Le Gal La Salle, M. David, Solar forecasts based on the clear sky index or the clearness index: which is better? in: Solar, vol. 2, MDPI, 2022, pp. 432–444.
[48] A. Martinez-Gracia, I. Arauzo, J. Uche, Solar energy availability, in: Solar Hydrogen Production, Elsevier, 2019, pp. 113–149.
[49] G. Kopp, J.L. Lean, A new, lower value of total solar irradiance: Evidence and climate significance, Geophys. Res. Lett. 38 (1) (2011).
[50] J.S. Stein, W.F. Holmgren, J. Forbess, C.W. Hansen, PVLIB: Open source photovoltaic performance modeling functions for Matlab and Python, in: 2016 IEEE 43rd Photovoltaic Specialists Conference, PVSC, IEEE, 2016, pp. 3425–3430.
[51] L. Cornejo-Bueno, C. Casanova-Mateo, J. Sanz-Justo, S. Salcedo-Sanz, Machine learning regressors for solar radiation estimation from satellite data, Sol. Energy 183 (2019) 768–775.
[52] I. Goodfellow, Y. Bengio, A. Courville, Deep Learning, MIT Press, 2016.
[53] A. Vaswani, N. Shazeer, N. Parmar, J. Uszkoreit, L. Jones, A.N. Gomez, Ł. Kaiser, I. Polosukhin, Attention is all you need, Adv. Neural Inf. Process. Syst. 30 (2017).
[54] Z. Niu, G. Zhong, H. Yu, A review on the attention mechanism of deep learning, Neurocomputing 452 (2021) 48–62.
[55] P. Kumari, D. Toshniwal, Deep learning models for solar irradiance forecasting: A comprehensive review, J. Clean. Prod. 318 (2021) 128566.
[56] T. O'Malley, E. Bursztein, J. Long, F. Chollet, H. Jin, L. Invernizzi, et al., KerasTuner, 2019, https://github.com/keras-team/keras-tuner.
[57] J.M. Bright, X. Sun, C.A. Gueymard, B. Acord, P. Wang, N.A. Engerer, Bright-Sun: A globally applicable 1-min irradiance clear-sky detection model, Renew. Sustain. Energy Rev. 121 (2020) 109706.
[58] Y. Xie, M. Sengupta, J. Yang, A. Habte, G. Buster, B. Benton, M. Foster, A. Heidinger, Y. Liu, The influence of cloud cover on the reliability of satellite-based solar resource data, Renew. Sustain. Energy Rev. 208 (2025) 115070.